On the time-dependent radiative transfer in photospheric plasmas. II. The analytical theory versus Monte Carlo

On the time-dependent radiative transfer in photospheric plasmas: II. The analytical theory versus Monte Carlo

August L Schultz and Martin A Schweizer†

Department of Physics, 201 North Physics Building, University of Utah, Salt Lake City, UT 84112, USA

Abstract. This paper is the second of a series investigating time-dependent radiative transfer processes of x-rays in photospheric plasmas. We present a quantitative discussion of analytical results derived earlier and a comparison with Monte Carlo simulations. The geometry considered here is a homogeneous plasma ball with radius R. The source is concentrated on a concentric shell with radius $r_0 < R$. Point sources at the centre of the ball or semi-infinite geometries are discussed as limiting cases. The time profile for the source can be arbitrary. Diffusion profiles are given for every scattering order and the total profile appears as the sum over these individual profiles. The comparison with Monte Carlo results is used to test the accuracy of the analytical approach and to adjust the time profiles of the first few scattering orders. The analytical theory yields good results over a wide range of situations with remarkable numerical efficiency. All results can be calculated on a microcomputer.

1. Introduction

This paper is the second in a series investigating time-dependent radiative transfer processes of x-rays in photospheric plasmas. By photospheric we mean that the photon lifetimes with respect to absorption are larger than the typical escape times; see the introduction to Schweizer (1987, hereafter referred to as I). The purpose of this second paper is to discuss the analytical results derived in I and to compare them with numerical simulations.

The work presented here marks progress in several ways. The analytical results are given as explicit solutions of a random walk process in $(1+3)$ dimensions and the numerical part is reduced to the straightforward task of performing one-dimensional convolution integrals of polynomial Green functions with an arbitrarily chosen time profile $\sigma(t)$ for the source. The numerical efficiency is remarkable; all results can be calculated on a microcomputer.

Most of the earlier analytical treatments are based on the so-called two-stream approximation and provide models for one-dimensional media only, see, e.g., Code (1964) or Nagel and Mészáros (1985).

The general geometry considered here is a homogeneous plasma ball with radius R. The source is concentrated on a concentric shell with radius $r_0 < R$. For $r_0/R \ll 1$, we obtain the case of a point-like source at the centre of the ball. The opposite limit is reached if $(R - r_0)/R \ll 1$. This corresponds to a semi-infinite geometry with source at optical depth $\tau_0 = R - r_0$ below the boundary.

Although our analytical results are based on symmetry assumptions they account for the three dimensionality of the transfer problem. The photons in our model always move on a thermal cone in spacetime. The thermal cone for unscattered photons coincides with the future light cone in Minkowski space. This corresponds to a characteristic velocity $v_c = c = 3 \times 10^{10}$ cm s^{-1}. The three-dimensionality becomes apparent for many-times scattered photons; the thermal cone narrows down to an opening corresponding to $v_c = (1/\sqrt{3})c$. Section 4 is devoted to the question of how the thermal cone must be chosen for every scattering order.

The applicability of transport equations to rapidly varying sources or to geometries of modest optical depth is not necessarily obvious. For this reason we did not feel compelled to compare our findings with alternative analytical methods or results obtained from numerical integration of the Boltzmann equation; see Guilbert (1981) or Kunasz (1983). We decided, instead, to use the most fundamental test available and simulate every step numerically.

The comparison with Monte Carlo simulations serves two functions. First it provides a means to test the accuracy of the analytical results and second it allows us to adjust the thermal cone in each scattering order; see § 4 below. The total diffusion time profile $P(t)$ for a given situation is the sum over all scattering orders, i.e.

$$P(t) = \sum_{N=0}^{\infty} P_N(t) \tag{1}$$

where $P_N(t)$ is the profile of the N-times scattered photons. It is shown in § 4 how information inferred from the Monte Carlo results can be used to adjust the first few P_N.

The Monte Carlo simulations, which include all geometrical details of Thomson scattering in three dimensions, produce the same results if Thomson scattering is replaced by perfectly isotropic scattering. This partially explains why the analytical theory, which treats all scatterings as isotropic, produces good results over a wide range of situations.

This paper is organised as follows. In § 2, the main analytical result describing an extended shell source inside a plasma ball is introduced. Section 3 gives a description of the Monte Carlo methods applied in this work. Section 4 deals with the adjustment of the thermal cone for the first few P_N. In §§ 5 and 6, we study semi-infinite geometry and point sources, respectively. Section 7 details the modifications in the Monte Carlo algorithm required for the simple case of a constant absorption coefficient.

The format and timescale of related figures compared in the text are always the same. The interested reader may conveniently examine the details by copying corresponding graphs onto a transparency.

2. The scattering orders for a source with finite radius

The geometries discussed in this paper are homogeneous plasma balls with radius R. By homogeneous we mean that the matter density, the chemical composition, and in particular the electron number density n_e are the same everywhere. The mean free path $\lambda_T = \kappa_T^{-1} = (n_e \sigma_T)^{-1}$ of a photon with respect to Thomson scattering is therefore a constant in space and time. We set the speed of light equal to unity and introduce the following dimensionless time and space variables:

$$t \equiv \kappa_T t \qquad x \equiv \kappa_T x.$$

In the general case a source

$$S(t, x) = \delta(r - r_0)\delta(t) \tag{2}$$

concentrated on a shell with radius $r_0 \leq R$, releases photons isotropically. The shape of the time profile $\delta(t)$ of the source can, in principle, be arbitrary. The discussion below will show, however, that the analytical approach is not valid for very rapidly varying sources.

It was pointed out in the introduction of I that we are primarily interested in so-called *photospheric* plasma geometries, i.e. those in which Thomson scattering dominates the radiative transfer and absorption plays a secondary role. Absorption effects are nevertheless included in our approach and some aspects are discussed in § 7. For any radiative absorption coefficient κ_a we define a dimensionless version $a \equiv \kappa_a \kappa_T^{-1}$ characterising the inverse of the absorption time in units of the Thomson mean collision time $t_T = \kappa_T^{-1}$.

Let us assume that a source of the type defined in (2) releases a flash of photons according to an unspecified time profile $\delta(t)$. An observer positioned at radius $r \leq R$ will notice this flash as a signal profile $P(t)$ such as indicated in (1), where $P_N(t)$ is the time profile of the N-times scattered photons arriving at r. Most important is the case $r = R$ characterising the escape of photons from the plasma ball. Since all scatterings of photons with electrons are treated as isotropic, the emission from the surface is also isotropic and, modulo a geometric factor, given by $P_N(t)$.

It is easy to see from equations (44), (45), (48) and appendix 1 in I that the individual scattering orders are given by

$$P_{N-1}(t, R, r, r_0; \chi; a)$$

$$= \chi \frac{r_0}{r} \left(\frac{1}{2}\right)^N \exp[-(1+a)t] \sum_{\nu=1}^{N} \frac{EV(\nu-1)}{\{[(\nu-1)/2]!\}^2}$$

$$\times \left[\int_{-\infty}^{t-\chi|r-r_0|} dt' \frac{(t-t')^{N-\nu}}{(N-\nu)!} \left(\frac{(t-t')^2 - \chi^2(r-r_0)^2}{4}\right)^{(\nu-1)/2} \exp[(1+a)t']\delta(t') \right.$$

$$\left. - \int_{-\infty}^{t-\chi(r+r_0)} dt' \frac{(t-t')^{N-\nu}}{(N-\nu)!} \left(\frac{(t-t')^2 - \chi^2(r+r_0)^2}{4}\right)^{(\nu-1)/2} \exp[(1+a)t']\delta(t') \right]$$

$$+ \chi \frac{r_0}{r} \left(\frac{1}{2}\right)^N \exp[-(1+a)t] \sum_{\nu=2}^{N \geq 2} \sum_{n=1}^{\nu-1} \frac{EV(\nu-n-1)}{[(\nu-n-1)/2]! \, [(\nu+n-1)/2]!}$$

$$\times \left[\int_{-\infty}^{t-2n\chi R+\chi|r-r_0|} dt' \frac{(t-t')^{N-\nu}}{(N-\nu)!} \left(\frac{(t-t')^2 - (2n\chi R - \chi|r-r_0|)^2}{4}\right)^{(\nu-n-1)/2} \right.$$

$$\times \left(\frac{t-t'-2n\chi R + \chi|r-r_0|}{2}\right)^n \exp[(1+a)t']\delta(t')$$

$$+ \int_{-\infty}^{t-2n\chi R-\chi|r-r_0|} dt' \frac{(t-t')^{N-\nu}}{(N-\nu)!} \left(\frac{(t-t')^2 - (2n\chi R + \chi|r-r_0|)^2}{4}\right)^{(\nu-n-1)/2}$$

$$\times \left(\frac{t-t'-2n\chi R - \chi|r-r_0|}{2}\right)^n \exp[(1+a)t']\delta(t')$$

$$- \int_{-\infty}^{t-2n\chi R+\chi(r+r_0)} dt' \frac{(t-t')^{N-\nu}}{(N-\nu)!} \left(\frac{(t-t')^2 - [2n\chi R - \chi(r+r_0)]^2}{4}\right)^{(\nu-n-1)/2}$$

$$\times \left(\frac{t - t' - 2n\chi R + \chi(r + r_0)}{2} \right)^n \exp[(1+a)t']\jmath(t')$$

$$- \int_{-\infty}^{t - 2n\chi R - \chi(r + r_0)} dt' \frac{(t-t')^{N-\nu}}{(N-\nu)!} \left(\frac{(t-t')^2 - [2n\chi R + \chi(r + r_0)]^2}{4} \right)^{(\nu - n - 1)/2}$$

$$\times \left(\frac{t - t' - 2n\chi R - \chi(r + r_0)}{2} \right)^n \exp[(1+a)t']\jmath(t') \Bigg] \tag{3}$$

where

$$EV(n) = \begin{cases} 1 & n = 0, 2, 4, 6, \ldots \\ 0 & \text{otherwise.} \end{cases}$$

For all but the lowest scattering orders, the so-called characteristic parameter χ, which is basically the inverse of the characteristic velocity v_c, must be set equal to $\sqrt{3}$. A detailed discussion of this is presented in § 4.

We have, so far, studied Gaussian-type source profiles $\jmath(t) = \exp(-\alpha t^2)$. The scale of the time variation of such a source is of order

$$\frac{1}{\sqrt{\alpha}} \equiv \frac{1}{\sqrt{\alpha}} t_T.$$

The case of rapidly varying sources, the so-called Knudsen regime, is particularly delicate. We shall see below that the low scattering orders, predicted by the analytical theory, are inaccurate if $\alpha \gg 1$. This is especially true for small-sized sources $r_0 \leq 1$.

Figures 1, 2 and 3 illustrate the example of a shell source $r_0 = 5$ inside a ball $R = 10$. Absorption is neglected, i.e. $a = 0$. The choice of $\alpha = 0.05$ for the Gaussian parameter corresponds to a scale of 4.5 t_T for the time variation of the source. This is an extremely short time in most astrophysical situations. The intensity profiles shown in this example are for an observer at $r = R$.

Figure 1(c) shows the first dozen scattering orders contributing to the diffusion front. These profiles have been adjusted according to the rules to be introduced in § 4.

Figure 2(a) illustrates the development of the higher scattering orders; P_5, P_{10}-P_{60} are given. Starting at about $N = 20$, the position of max P_N is roughly at $t = N$. The precision of this correlation improves with increasing N. This general effect can be explained by the large optical thickness of the ball which causes the many-times scattered photons to mimic a Poissonian time distribution such as is known in the infinite medium case; see § 2 in I.

Figure 3(a) shows the sum (1) for this example. All orders P_0-P_{255} are included. Higher scattering orders are numerically insignificant and do not contribute to $P(t)$ for $t \leq 130$. The optical depth of the source below the boundary is 5 units. This implies an average escape time $t_e < 25 \; t_T$, roughly explaining the position of the peak and the decay of the profile.

Expression (3) includes a double sum over the two indices ν and n. The index n essentially counts the number of times a photon could possibly have crossed through the plasma ball before escaping at time t; see the original results in terms of Heaviside functions given in I. In the case of the example discussed above it is, for instance, possible to restrict the summation over the index n to $n \leq n_{max}$ as follows: $n_{max} = 1$ for $t \leq 30$, $n_{max} = 2$ for $t \leq 60$, $n_{max} = 3$ for $t \leq 100$ and $n_{max} = 4$ for $t \leq 130$.

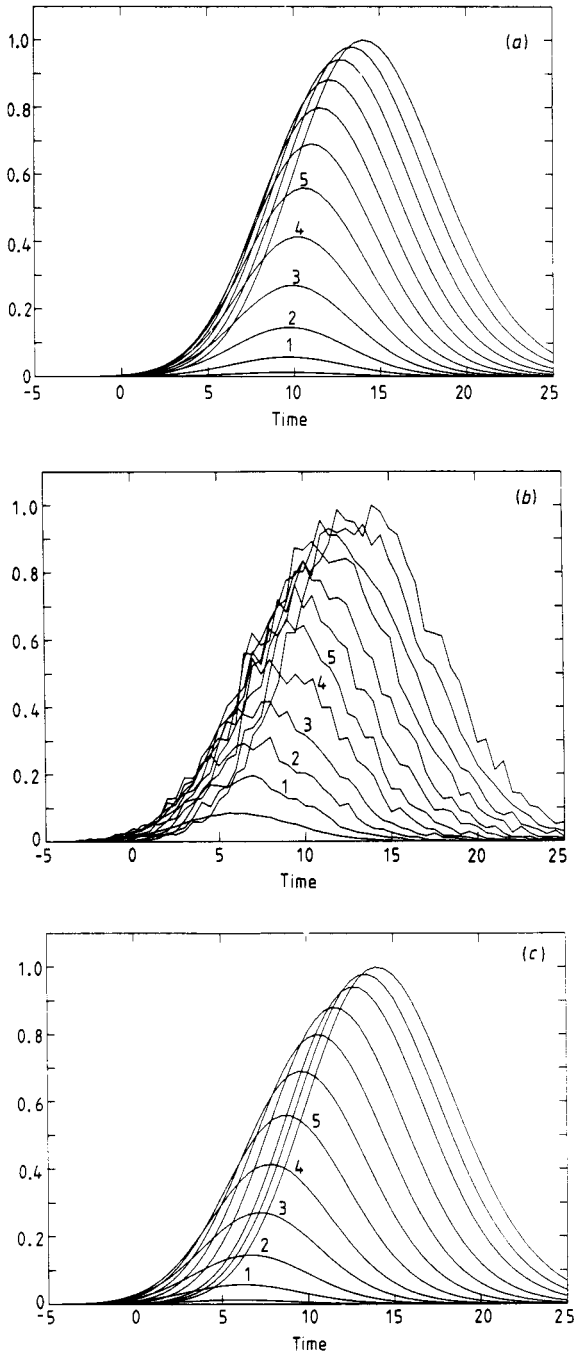**Figure 1.** The profiles P_0-P_{11} as functions of $t \equiv t\, t_T^{-1}$ for the case of a shell source $r_0 = 5$ inside a ball $R = 10$. The magnitudes have been normalised to a scale running from zero to unity. There is no absorption and $\alpha = 0.05$. The peaks grow with increasing N and the individual P_N can easily be identified. The observer is at the boundary, i.e. at $r = R$. In (a), we show the case $\chi = \sqrt{3}$ for all orders. The profiles in (b) are from our numerical simulation for the same case. The analytical profiles in (c) have been adjusted according to the two rules given in § 4.
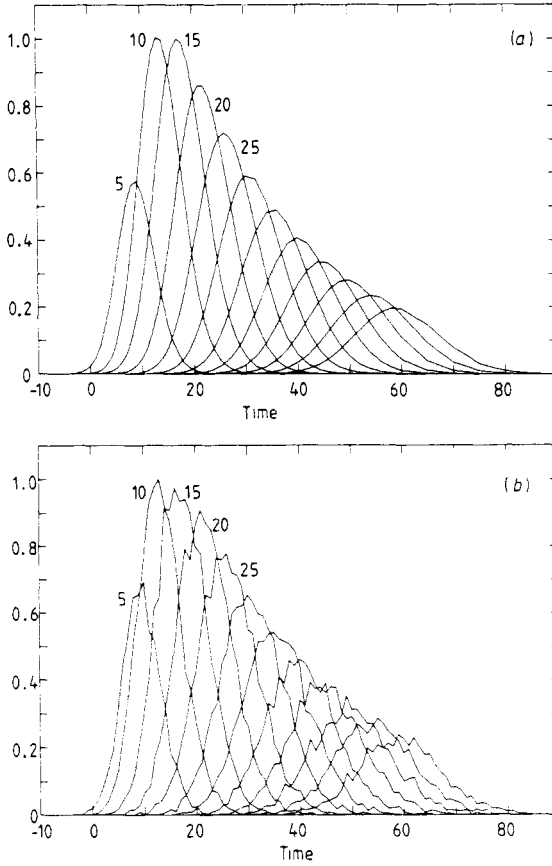
Figure 2. The profiles P_5, $P_{10}-P_{60}$, for the same geometry as in figure 1, are shown in (a) from the analytical theory and in (b) from our Monte Carlo simulation. The peaks are progressively delayed with N increasing and the individual P_N can easily be identified.

3. Numerical simulations of time-dependent photodiffusion processes

The Monte Carlo method simulates the random walk of a photon inside a plasma geometry. In a general situation, this includes keeping track of a photon's energy, path length and location, and the number of scatterings it has suffered. A photon absorbed by the plasma after N scatterings is discounted and does not contribute to the $(N+1)$th scattering order. The random walk of a photon is basically a repeating sequence of two processes: propagation along a trajectory and subsequent scattering by an electron encountered on that trajectory, i.e. Compton scattering.

The photon trajectories considered in this paper are null geodesics in a flat space-time, i.e. we do not allow for gravitational light deflection or gravitational redshift. When projected down to 3-space, a photon trajectory extends as a straight line along an arbitrary axis in 3-space. Let us label the positions along such an axis with x. Furthermore, let us assume that the starting point of such a trajectory is at $x = 0$, that it terminates at some position $x > 0$, and that there are *no boundaries*. Boundaries are included later in this section. The terminal position x is generated numerically from a probability density function $T(x)$ describing the relative number of trajectory
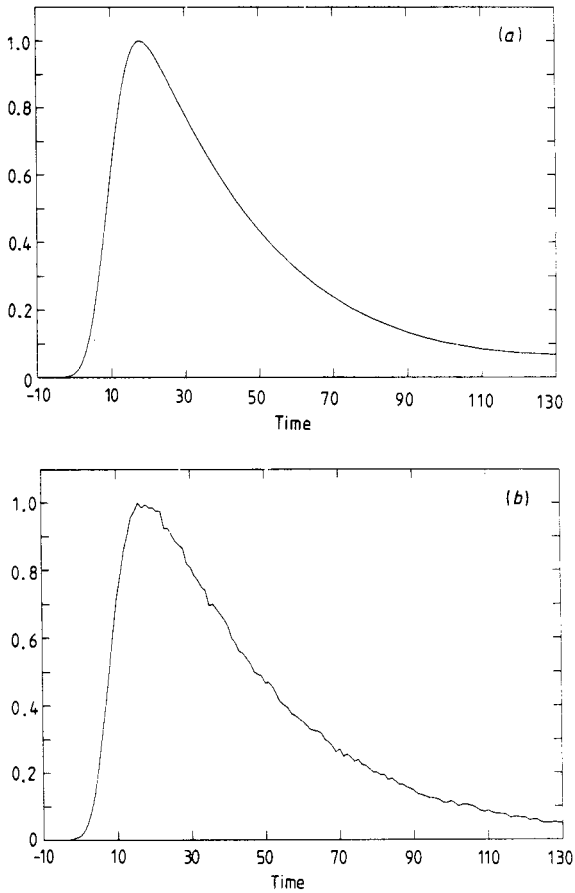
Figure 3. The sum over P_0-P_{255}, for the same geometry as in figure 1, is shown in (a) for the analytical theory. The diffusion profile predicted by our Monte Carlo method is shown in (b).

endpoints per unit length on the positive x axis; notice that $T(x) = 0$ for $x < 0$. The probability $p(x)$ that a photon reaches some value $x > 0$ is given by the cumulative probability that its trajectory terminates at a position $y > x$, i.e.

$$p(x) = \int_x^\infty \mathrm{d}y \, T(y). \tag{4}$$

Suppose a photon trajectory terminates at $x > 0$; there are two possibilities.

(i) the photon is absorbed by the plasma at x and discounted in the further evolution of the diffusion process.

(ii) The photon is scattered into a new direction with new energy. For electrons at relativistic temperatures, $kT \sim m_e c^2$, interacting with high-energy photons, $h\nu \sim m_e c^2$, the scattering cross section is energy dependent and the energy shift on scattering can be significant. However, since we are interested in clearly non-relativistic electron temperatures and photon energies, we take the electrons to be fixed and generate the scattering direction from the probability density function defined by the Thomson

cross section, i.e. from

$$TH(\mu) = \begin{cases} \frac{3}{8}(1+\mu^2) & -1 \le \mu \le 1 \\ 0 & \text{otherwise} \end{cases} \tag{5}$$

where $\mu = \cos \theta$, and θ denotes the angle between incident and scattered direction of the photon. The energetic effects of Compton scattering will be included in the next paper of this series.

This clarifies the simulation of the scattering process and we now turn to the question of the explicit form of $T(x)$. The geometries considered in this paper are homogeneous, thus defining a constant mean free path $\bar\lambda$. Invoking arguments from kinetic theory, one arrives at the conclusion that

$$T(x) = \begin{cases} \bar\lambda^{-1} \exp(-x/\bar\lambda) & x > 0 \\ 0 & \text{otherwise}^\dagger \end{cases} \tag{6}$$

(see, e.g., § 59 in Kennard (1938)).

Let us give an alternative argument leading to the form (6). We assume that N_0 photons move from $x = 0$ in the positive x direction. We choose two points $\Delta > x > 0$. The number of trajectories terminating in the interval $[0, x]$ is given by

$$N_0 \int_0^x dy\, T(y). \tag{7}$$

Thus, the number of trajectories which extend beyond x is given by

$$N(x) = N_0 \left[1 - \int_0^x dy\, T(y) \right].$$

These surviving photons give rise to $N(x)$ trajectories starting at x. The translational invariance of the infinite medium implies that the probability density function associated with trajectories starting at x is given by $T(y - x)$. We conclude from this that

$$N(x) \int_x^\Delta dy\, T(y - x) \tag{8}$$

is the number of trajectories terminating in the interval $[x, \Delta]$. The total number of trajectories terminating in the interval $[0, \Delta]$ is the sum of (7) and (8). Since this total number can be given directly as

$$N_0 \int_0^\Delta dy\, T(y)$$

we arrive at the following equation:

$$\int_0^\Delta dy\, T(y) = \int_0^x dy\, T(y) + \left(1 - \int_0^x dy\, T(y) \right) \int_x^\Delta dz\, T(z - x). \tag{9}$$

Some straightforward manipulations lead us to

$$T(x)\, T(\Delta - x) + \frac{T(\Delta)}{T(\Delta - x)} \frac{d}{d\Delta} T(\Delta - x) = 0. \tag{10}$$

For $x = 0$, equation (10) reduces to

$$\frac{d}{d\Delta} T(\Delta) = -T(0)\, T(\Delta)$$

which has the general solution

$$T(\Delta) = 1/l \exp(-\Delta/l) \qquad \Delta \geq 0. \tag{11}$$

Our argument does, of course, not fix the integration constant $l = T(0)^{-1}$ which is now identified with $\bar{\lambda}$.

Finally, let us sketch the algorithm for the case of a *point source* placed at the centre of a ball with radius R. Absorption is *neglected* at this point; see, however, § 7. The observer is positioned at the boundary of the ball.

The algorithm applied here is an adapted version of the modern Monte Carlo method introduced by Pozdnyakov *et al* (1977, 1979) in the context of Comptonisation of photons in optically thin but relativistically hot plasmas. This method is equivalent to the conventional treatment but numerically more efficient when rare events are responsible for the formation of the Comptonised spectra. This method has also been applied by Schultz and Price (1985) in their analysis of pair production in spherical accretion onto 'black holes'. Instead of following an individual photon until it reaches the boundary, the new method starts with a statistical weight N_0 which may be interpreted as a number of identical photons released from the source, say, at time $t = 0$.

The presence of a *spherical boundary* at $r = R$ divides the photon trajectories, originating inside the sphere, into two classes. Trajectories terminating in the interior of the ball describe photons which scatter. Trajectories terminating outside describe photons which escape. The endpoints of trajectories terminating inside are generated numerically from the probability density function (6) truncated at the boundary. The following steps are illustrated in figure 4.

(a) Determine the distance to the boundary: R.

(b) $N_0 \exp(-R/\lambda_T)$ photons reach the boundary at $t = R$ (see the derivation of (4)) and contribute to $P_0(t)$.
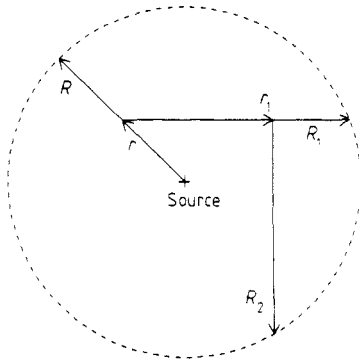

Figure 4. Illustration of the Monte Carlo algorithm discussed in § 3.

(c) $N_1 \equiv N_0[1 - \exp(-R/\lambda_T)]$ photons scatter at some point r. The position r is generated numerically from the probability density function

$$\lambda_T^{-1}[1 - \exp(-R/\lambda_T)]^{-1} \exp(-r/\lambda_T) \qquad 0 \leq r \leq R.$$

(d) The new direction of the scattered photons is obtained by generating μ from (5) and the azimuthal angle from the uniform distribution.

(a') Determine the distance to the boundary along the new direction: R_1.

(b') $N_1 \exp(-R_1/\lambda_T)$ photons reach the boundary at $t = r + R_1$ and contribute to $P_1(t)$.

(c') $N_2 = N_1[1 - \exp(-R_1/\lambda_T)]$ photons scatter at position r_1 generated from

$$\lambda_T^{-1}[1 - \exp(-R_1/\lambda_T)]^{-1} \exp(-r/\lambda_T) \qquad 0 \leqslant r \leqslant R_1.$$

(d') Determine new direction of scattered photons.

This sequence is continued until either the number N_i of photons remaining in the sphere is reduced below some predetermined value, or the scattering order i becomes equal to a predetermined maximum order, or the total path length, $t = \Sigma r_i$, equals a predetermined maximum. This algorithm includes all geometrical details of Thomson scattering in three dimensions. However, if we replace (5) by the uniform distribution in μ, thus simulating perfectly isotropic photon scatterings, we obtain virtually identical results. The uniform distribution in μ is given by

$$U(\mu) = \begin{cases} \frac{1}{2} & -1 \leqslant \mu \leqslant 1 \\ 0 & \text{otherwise.} \end{cases}$$

The intersection of the two areas defined by $TH(\mu)$ and $U(\mu)$ is equal to 0.903 775. The agreement between the two cases is therefore not surprising.

4. Treatment of the diffusion front

The scattering orders (3) have been obtained as a byproduct of solving the telegraphy equation

$$\frac{\partial}{\partial t} P + \frac{\partial^2}{\partial t^2} P - \chi^{-2} \Delta P = S. \tag{12}$$

The solution P is the sum over all scattering orders as indicated in (1). We may consider (12) as a hyperbolic diffusion equation, allowing for finite signal propagation only. The characteristic velocity associated with (12) is $v_c = \chi^{-1}$. It was pointed out in I that $v_c = 1/\sqrt{3}$ is reasonable for the description of many-times scattered photons. The photon momenta are randomly distributed in this case and there are no privileged spatial directions. The characteristic velocity in a given direction is then the root mean square of the photon velocity in that direction, i.e. $1/\sqrt{3} \cdot c \equiv 1/\sqrt{3}$. This picture does not apply to photons having suffered few collisions only. The characteristic velocity associated with unscattered photons is equal to c, i.e. $v_c = \chi^{-1} = 1$. For the first few scattering orders, the so-called characteristic parameter χ varies between unity and $\sqrt{3}$. Figure 5(a) shows P_{10}, P_{20}, P_{30}, P_{40}, P_{50} and P_{60} for two fixed choices of χ. The geometry is semi-infinite with the source at optical depth $\tau_0 = 10$ below the boundary. The Gaussian parameter is $\alpha = 0.05$. The broken curves represent the profiles for $\chi = 1$, and the full curves are the profiles for $\chi = \sqrt{3}$. In the $\sqrt{3}$ case, the orders P_{10}, P_{20}, P_{30} and P_{40} are visibly delayed compared to their ($\chi = 1$) counterparts. For $\chi = 1$, the peaks are maximal around P_{20} and decay rapidly thereafter. This contrasts with the $\sqrt{3}$ case where the peaks become maximal between P_{40} and P_{50}. There is also a visible discrepancy in the absolute magnitudes: max $P_{20}(\chi = 1)$ is about twice the value of max $P_{40}(\chi = \sqrt{3})$.

Figure 5(b) shows the same scattering orders produced from our numerical simulation. A comparison with figure 5(a) leaves no doubt that $\chi = \sqrt{3}$ is the proper choice. This is, in fact, generally true as far as high scattering orders are concerned.

The treatment of the low scattering orders, on the other hand, is more delicate. As pointed out above, the case P_0 calls for $\chi_0 = 1$. For the subsequent orders we expect
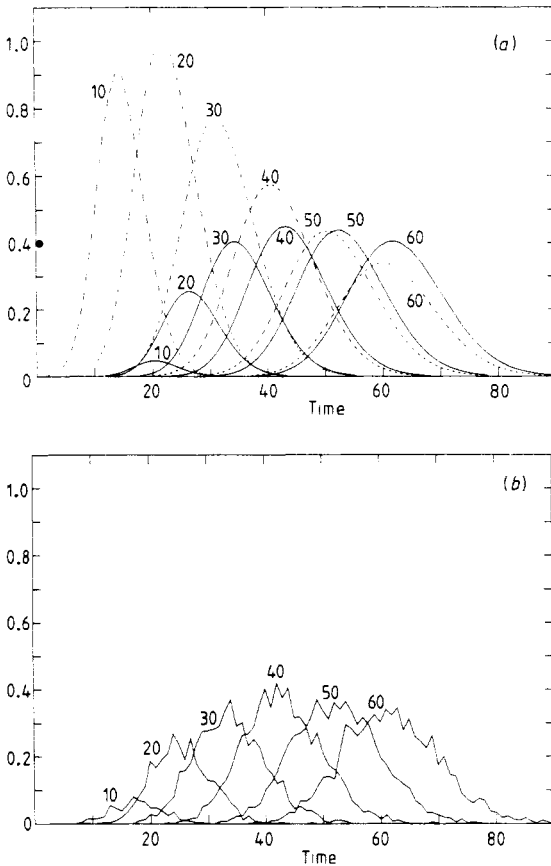
Figure 5. These figures show, from left to right, P_{10}, P_{20}, P_{30}, P_{40}, P_{50} and P_{60} for a source at optical depth $\tau_0 = 10$ below the boundary in a semi-infinite geometry. There is no absorption, $\alpha = 0.05$ and the observer is at the boundary, i.e. $\tau = 0$. The broken curves in (a) are analytical profiles for $\chi = 1$. The full curves show the same case for $\chi = \sqrt{3}$. The profiles in (b) are from our numerical simulation.

the χ_N to grow with increasing N and this sequence should eventually converge to $\sqrt{3}$. After studying many examples we found that the sequence $\chi_0 = 1$, $\chi_1 = 1.05$, $\chi_2 = 1.1$, $\chi_3 = 1.15$, $\chi_4 = 1.2$, $\chi_5 = 1.3$, $\chi_6 = 1.4$, $\chi_7 = 1.5$, $\chi_8 = 1.6$ and $\chi_N = \sqrt{3}$ for $N \geq 9$ guarantees reasonably good agreement with the Monte Carlo results and does so independently of the particulars of the geometry under consideration. Figure 5(a) shows that a shift in χ not only changes the timing of a profile but also its magnitude. As a second rule we have, therefore, decided to rescale the magnitudes of the P_N back to the values obtained for $\chi_N = \sqrt{3}$.

We do not intend to justify these rules on theoretical grounds. The difficulties encountered in connection with the diffusion front are of a fundamental nature, since our analytical results are solutions of a diffusion equation. A generic property of the diffusion regime is the $(1/r)$ decay behaviour of the perturbations. In fact, even the random distribution $W_1(t, x)$, upon which our analytical results are based, shows this behaviour; see (11) in I. Since W_1 is used to describe unscattered photons one would definitely wish it to decay like $(1/r^2)$. The diffusion equation (12), however, determines W_1 uniquely (see I) and it is an unfortunate fact that W_1 decays like $(1/r)$. This

compounds the complications with the low scattering orders. Applying our analytical results to the first few P_N amounts, in fact, to pushing the diffusion approximation beyond its range of validity. The two rules given above should be seen as a practical compromise which is not yet optimal. A more sophisticated procedure would make the adjustments consistently dependent on the type of geometry, optical depth and scattering order. However, the results obtained in this manner are already surprisingly good, fortunately good enough for all our future applications of this method.

Let us illustrate the adjustments with the following example. Figure 1(*a*) shows P_0-P_{11} for a shell source at optical depth 5 below the boundary of a ball with radius $R = 10$. We have set $\chi_N = \sqrt{3}$ for all these profiles. The very first scattering orders have their maxima near $t = 10$. With increasing N, the peaks move to the right with max P_{11} near $t = 15$. The Monte Carlo simulations graphed in figure 1(*b*) show, however, that the very first scattering orders should have their maxima near $t = 5$. The analytical profiles in figure 1(*c*) have been adjusted according to the two rules described above. The timing of the peaks in figure 1(*c*) is in excellent agreement with Monte Carlo. The magnitudes of P_0-P_5 appear, however, to be too small if compared to their counterparts in figure 1(*b*). With increasing optical depth the discrepancy between the magnitudes of the first few scattering orders becomes even greater, but decreases for smaller optical depths. Since the lowest P_N are numerically not very significant in the clearly optically thick case, this disagreement does not pose a serious problem. It should, in this context, be noticed that figures 3(*a*) and 3(*b*), showing the sum for the adjusted analytical and corresponding Monte Carlo case of our example, are in perfect agreement. This includes the onset of the diffusion profiles. Notice also the excellent agreement between figures 2(*a*) and 2(*b*). There is a visible but not dramatic discrepancy between the magnitudes of the P_5 profiles.

5. The semi-infinite medium

The case of a semi-infinite geometry is included in (3) as a limit. Let τ (or τ_0) denote the optical depth of the observer (or source) below the boundary at R, i.e. $r = R - \tau$ and $r_0 = R - \tau_0$. We substitute these expressions for r and r_0 into (3) and go to the limit of R approaching infinity. It follows that

$$P_{N-1}(t, \tau, \tau_0; \chi; a)$$

$$= \chi \left(\frac{1}{2}\right)^N \exp[-(1+a)t] \sum_{\nu=1}^{N} \int_{-\infty}^{t-\chi|\tau-\tau_0|} \mathrm{d}t' \frac{EV(\nu-1)}{\{[(\nu-1)/2]!\}^2} \frac{[t-t']^{N-\nu}}{(N-\nu)!}$$

$$\times \left(\frac{(t-t')^2 - \chi^2(\tau-\tau_0)^2}{4}\right)^{(\nu-1)/2} \exp[(1+a)t']\partial(t')$$

$$- \chi \left(\frac{1}{2}\right)^N \exp[-(1+a)t] \sum_{\nu=2}^{N \geqslant 2} \int_{-\infty}^{t-\chi(\tau+\tau_0)} \mathrm{d}t' \frac{EV(\nu-2)}{[(\nu-2)/2]!(\nu/2)!} \frac{(t-t')^{N-\nu}}{(N-\nu)!}$$

$$\times \left(\frac{(t-t')^2 - \chi^2(\tau+\tau_0)^2}{4}\right)^{(\nu-2)/2} \left(\frac{t-t' - \chi(\tau+\tau_0)}{2}\right) \exp[(1+a)t']\partial(t').$$

$$(13)$$

For large R, no photons diffusing through the plasma ball will reach the boundary on the other side after a finite amount of time. This explains why the original double

sum over the indices ν and n has been reduced to a single summation over ν with $n = 1$. The drastic reduction in the number of integrals makes (13) particularly attractive for applications. Fortunately, the convergence to the semi-infinite case is rapid. A shell geometry with given r_0 and R produces essentially the same profiles as a semi-infinite geometry with $\tau_0 = R - r_0$ if the ratio R/τ_0 is of order ten. In the example illustrated in figures 1, 2 and 3, the ratio $R/(R - r_0)$ is exactly equal to two. We have studied the corresponding semi-infinite geometry with $\tau_0 = 5$ and found only minor modifications of the profiles.

One expects the analytical theory to produce good results for optically thick cases. Surprisingly, the agreement with Monte Carlo extends down to even modest optical depths. Figure 6(a) shows P_0-P_{11} for a source at optical depth $\tau_0 = 1$, with $\alpha = 0.05$ and $a = 0$. These profiles are in excellent agreement with their Monte Carlo counterparts in figure 6(b). The inversion max $P_0 <$ max $P_1 >$ max P_2 is typical for the transition regime between optically thin and thick. The sum in Figure 7(a) includes P_0-P_{45}. It is a perfect match for the Monte Carlo counterpart in figure 7(b).

Discrepancies become visible in the optically thin regime. Figure 8(a) shows P_0-P_{11} for $\tau_0 = 0.1$, with $\alpha = 0.05$ and $a = 0$. When compared to the corresponding Monte
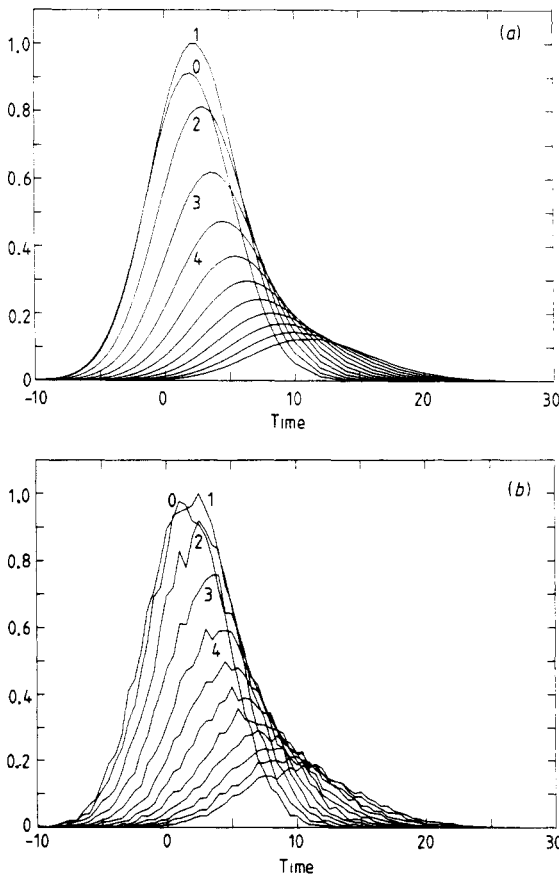

Figure 6. Semi-infinite geometry with $\tau_0 = 1$, $\alpha = 0.05$, $a = 0$ and $\tau = 0$. The orders P_0-P_{11} are shown. Notice the inversion in the sequence P_0, P_1, P_2. The profiles in (a) are from the analytical theory. The corresponding Monte Carlo profiles are shown in (b).
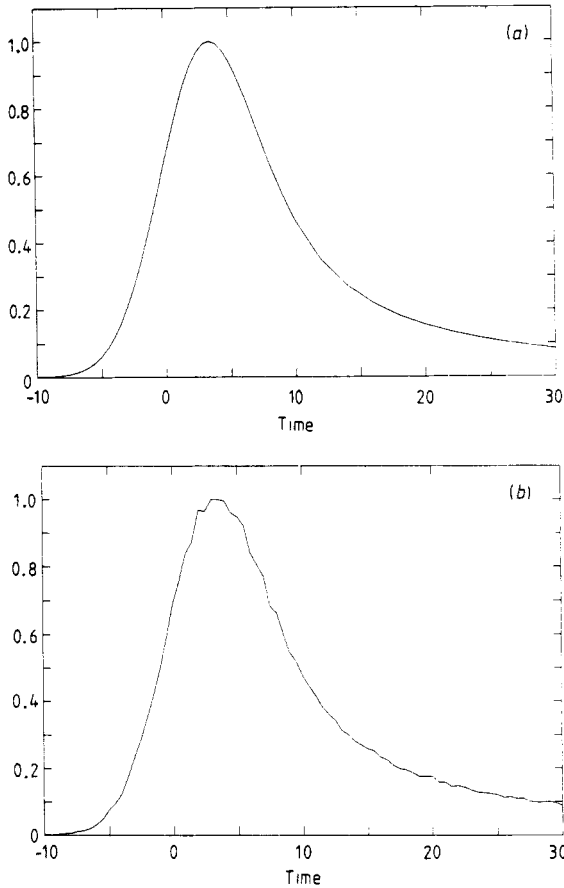
Figure 7. The analytical sum over P_0-P_{45} is shown in (a) for the same geometry as in figure 6. The corresponding Monte Carlo sum is shown in (b).

Carlo simulations in figure 8(b), these profiles appear to be slightly delayed, and the magnitudes are not in agreement. The discrepancy between the analytical sum and the Monte Carlo counterpart for this case is, on the other hand, not large. The analytical sum is delayed by one time unit but the shapes of the curves match perfectly.

In the case of extended sources $r_0 > 1$, the analytical results are applicable to the modest Knudsen regime, i.e. to sources with $1 \leqslant \alpha$. In figure 9(a) the front profiles P_0-P_{11} are shown for a semi-infinite geometry with $\tau_0 = 5$ and $\alpha = 5$. The comparison with our numerical simulations in figure 9(b) shows good agreement for the timing of the peaks, but the same discrepancy with the magnitudes of the very first P_N is visible. The analytical and Monte Carlo sums for this case match perfectly.

6. Point-like sources

In this section, we study the profiles of shell sources (2) with small radii $r_0 \ll 1$. For r_0 approaching zero such sources can be represented as

$$S(t, x) = \delta^3(x)\sigma(t). \tag{14}$$
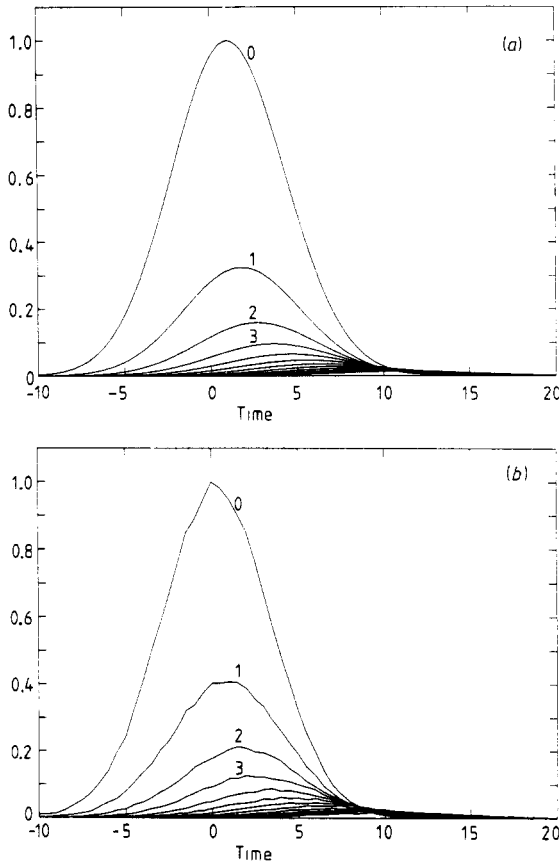
Figure 8. Semi-infinite geometry with $\tau_0 = 0.1$, $\alpha = 0.05$, $a = 0$ and $\tau = 0$. From top to bottom, the orders P_0-P_{11} are shown. The analytical profiles in (a) are delayed by about one time unit when compared to their Monte Carlo counterparts in (b).

The passage to the limit of a point source has been discussed earlier; see expression (5) in I. It is straightforward to obtain the following time-convoluted version of that result:

$$P_{N-1}(t, R, r; \chi; a)$$

$$= \frac{\chi^2}{4\pi r} \exp[-(1+a)\chi r] \frac{(\chi r/2)^{N-1}}{(N-1)!} \delta(t - \chi r)$$

$$+ \frac{\chi^2}{8\pi} \left(\frac{1}{2}\right)^N \exp[-(1+a)t] \left[\sum_{\nu=3}^{N} \int_{-\infty}^{t-\chi r} dt' \frac{(t-t')^{N-\nu}}{(N-\nu)!} \frac{EV(\nu-1)}{\{[(\nu-1)/2]!\}^2} \right.$$

$$\times (\nu-1) \left(\frac{(t-t')^2 - \chi^2 r^2}{4} \right)^{(\nu-3)/2} \exp[(1+a)t'] \delta(t') \right]$$

$$-\chi^2 \left(\frac{1}{2}\right)^N \exp[-(1+a)t]$$

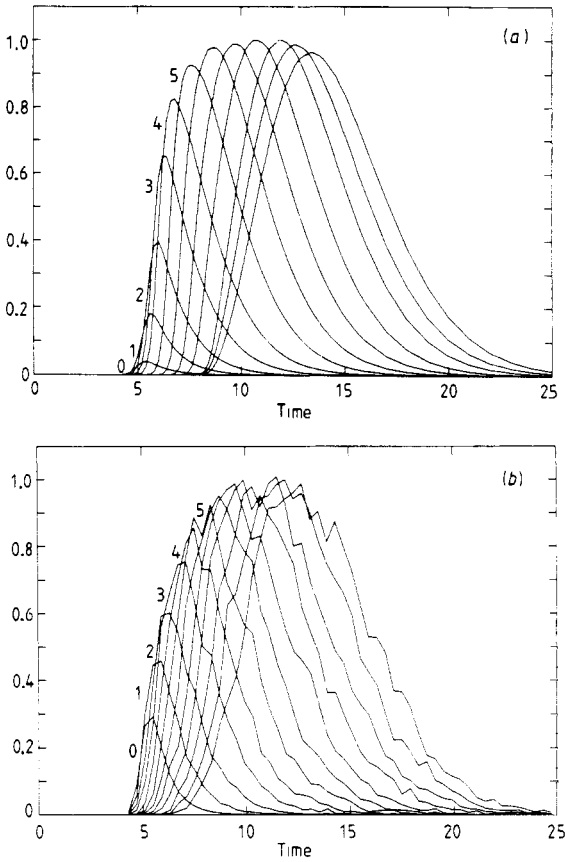$$\times \sum_{\nu=2}^{N} \sum_{n=1}^{\nu-1} \frac{EV(\nu-n-1)}{[(\nu-n-1)/2]![(\nu+n-1)/2]!} \frac{1}{(N-\nu)!}$$

Figure 9. Illustration of the Knudsen regime for a semi-infinite geometry with $\tau_0 = 5$, $a = 0$, $\tau = 0$, but $\alpha = 5$. The orders P_0-P_{11} are shown, in (a) from the analytical theory and in (b) from our numerical simulation.

$$\times \left[\int_{-\infty}^{t-2n\chi R + \chi r} dt' (2n\chi R - \chi r) \right.$$

$$\times \frac{(t-t')^{N-\nu}}{8\pi r} \left(\frac{(t-t')^2 - (2n\chi R - \chi r)^2}{4} \right)^{(\nu-n-3)/2}$$

$$\times \left(\frac{t-t'-2n\chi R + \chi r}{2} \right)^n (\nu - n - 1) \exp[(1+a)t'] \sigma(t')$$

$$+ \int_{-\infty}^{t-2n\chi R + \chi r} dt' \frac{(t-t')^{N-\nu}}{4\pi r} \left(\frac{(t-t')^2 - (2n\chi R - \chi r)^2}{4} \right)^{(\nu-n-1)/2} n$$

$$\times \left(\frac{t-t'-2n\chi R + \chi r}{2} \right)^{n-1} \exp[(1+a)t'] \sigma(t')$$

$$- \int_{-\infty}^{t-2n\chi R - \chi r} dt' (2n\chi R + \chi r) \frac{(t-t')^{N-\nu}}{8\pi r} \left(\frac{(t-t')^2 - (2n\chi R + \chi r)^2}{4} \right)^{(\nu-n-3)/2}$$

$$\times \left(\frac{t-t'-2n\chi R - \chi r}{2} \right)^n (\nu - n - 1) \exp[(1+a)t'] \sigma(t')$$

$$-\int_{-\infty}^{t-2n\chi R-\chi r} dt' \frac{(t-t')^{N-\nu}}{4\pi r} \left(\frac{(t-t')^2-(2n\chi R+\chi r)^2}{4}\right)^{(\nu-n-1)/2} n$$

$$\times \left(\frac{t-t'-2n\chi R-\chi r}{2}\right)^{n-1} \exp[(1+\alpha)t']\sigma(t')\bigg]. \tag{15}$$

This expression produces good results when applied to non-transient sources (i.e. $\alpha \leqslant 0.05$) in optically thick geometries. As we can tell from (12) in I, the photons scattering in the forward direction only are separately accounted for by a $\delta(t-\chi r)$-type precursor part. For the case of clearly transient sources with $\alpha > 1$, this singular part may dominate the other terms and give rise to exotic features in the onset portion of a diffusion profile. Figure 10(a) shows P_0-P_{11} for a point source at the centre of a ball with radius $R = 5$. The source is transient with $\alpha = 5$. The singular character of the precursor part becomes visible in the sharply peaked shapes of P_0-P_8. The sum for this case is shown in figure 10(b). The spikes give rise to a precursor at $t = 5$ clearly separated from the main peak near $t = 10$. The numerical simulations show, on the other hand, no such exotic features for $\alpha = 5$; see figure 10(c). However, if we consider an extremely transient source with, say, $\alpha = 100$, the Monte Carlo method produces a precursor strikingly similar to the analytical version with $\alpha = 5$; see figure 10(d).

The qualitative picture obtained from the analytical approach is, therefore, correct. The collapse of the quantitative accuracy is explained by the singular character of the random distributions the result (15) is based on. For an extended source, the spatial convolution integrals smear out the singular $\delta(t-\chi r)$ terms. This explains, for instance, why the results for the semi-infinite geometry are equally good for $\alpha = 5$ and $\alpha = 0.05$; see figure 9. The complications with the diffusion front associated with sources of type (14) persist if we give the source a small but finite extension $0 < r_0 < 1$ and proceed with (3). Applicability of the analytical theory to the Knudsen regime requires $r_0 > 1$. Expression (15) also produces inaccurate results when applied to cases of modest optical depth, say $R < 4$.

Figure 11(a) shows the sum P_0-P_{63} for an observer at $r = 5$ *inside* a ball with $R = 7$. the agreement with the Monte Carlo simulations is excellent; see figure 11(b). The peak in figure 11 is near $t = 15$ and the tail extends out to $t = 65$. This contrasts with the case $R = r = 5$ where the peak is near $t = 10$ and the tail only extends out to $t = 50$; see, for instance, the main peak and tail in figure 10(b). The delay of the peak and the extension of the tail in figure 11 are explained by the inside position of the observer which receives a delayed signal from the photons scattering inward from the domain between $r = 5$ and $R = 7$. If we increase the size of the ball to, say, $R = 50$, the profiles obtained at $r = 5$ agree with those obtained at $r = 5$ in an *infinite* medium. The peak is still near $t = 15$ but the diffusion tail extends out to $t = 200$.

The transition to a point source is a smooth one. For instance, the diffusion profiles of a shell source $r_0 = 1$ inside a ball $R = 10$ coincide with the diffusion profiles from a point source (14) at the centre of the same ball. In cases of very large R one may, therefore, model point sources with (3) and a source of finite extension.

7. Effects of absorption

The photospheric plasma geometries we are interested in are characterised by long photon lifetimes with respect to absorption. The effects of absorption become important if the optical depth of the source below the boundary is large (see in this context the review in the introduction to I). The absorption coefficients generally depend on the
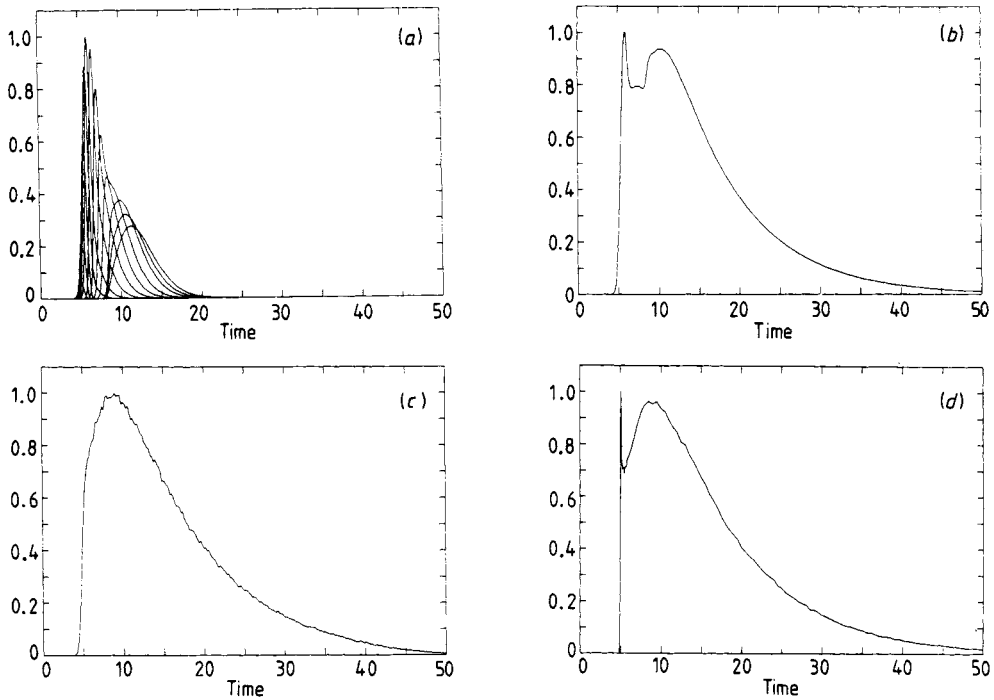
Figure 10. Knudsen regime for a point source at optical depth $R = 5$. In (a) P_0 through P_{11} are shown for the analytical theory with $\alpha = 5$ and $r = R$. The sum for this case is shown in (b) and includes P_0 through P_{65}. The Monte Carlo counterpart in (c) shows, however, no precursor for $\alpha = 5$. A similar profile can be produced from a numerical simulation if the transient parameter is increased to the high value $\alpha = 100$; see (d).

photon frequency and plasma temperature thus implying the same dependences for the dimensionless coefficient $a = \kappa_a / \kappa_T$. Every photon–electron scattering changes the photon frequency and the coefficient a must, in principle, be adjusted after every scattering. A full-scale discussion, covering Comptonisation plus absorption, will be presented in the next paper of this series. We are, at this point, only concerned with the simple case of a constant absorption coefficient $a < 1$.

The algorithm described in §3 needs some minor modifications. The mean free path λ_T in step (b) must be replaced by

$$\bar{\lambda} = (\kappa_T + \kappa_a)^{-1}.$$

As for step (c), it is clear that the remaining

$$N_0[1 - \exp(-R/\bar{\lambda})] \tag{16}$$

photons have two options. Either they are absorbed or they scatter at some point in the interval $[0, R]$. The point of scattering, r, is generated from the original probability density function

$$\lambda_T^{-1}[1 - \exp(-R/\lambda_T)]^{-1} \exp(-r/\lambda_T) \qquad 0 \le r \le R. \tag{17}$$

A fraction of the photons in (16) is lost in the interval $[0, r]$ due to absorption. Only

$$N_1 = \exp(-r\kappa_a) N_0[1 - \exp(-R/\bar{\lambda})]$$

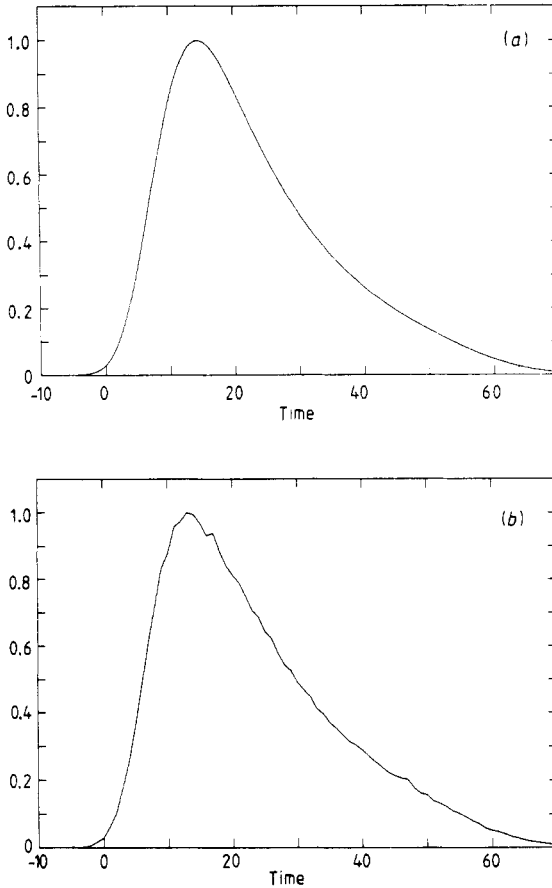photons reach the position r and are scattered as in step (d).

Figure 11. Profiles of a point source at the centre of a ball $R = 7$. The observer is *inside* at $r = 5$ and $\alpha = 0.05$. The sum over P_0-P_{63} is shown, in (a) from the analytical theory and in (b) from our numerical simulation.

The *conventional* Monte Carlo method handles absorption during the ith scattering by selecting a scattering point $r_s(i)$ from $\lambda_T^{-1} \exp(-r/\lambda_T)$, the density (16), and an absorption point $r_a(i)$ from the density $\kappa_a \exp(-\kappa_a r)$. For $r_a(i) < r_s(i) < R_i$ or $r_a(i) < R_i < r_s(i)$, the photon is absorbed and the trajectory terminated; R_i is defined as in § 3. For $r_s(i) < r_a(i) < R_i$ or $r_s(i) < R_i < r_a(i)$, the photon scatters ar $r_s(i)$ as in step (d) in § 3. For $r_s(i)$, $r_a(i) > R_i$, the photon escapes and is added to the output profile.

We have compared the two Monte Carlo methods and found them to be in perfect agreement.

Figure 12 shows the total diffusion profiles of a source at optical depth $\tau_0 = 10$ below the boundary of a semi-infinite geometry. The upper curve shows the case without absorption. The diffusion tail extends far beyond $t = 300$. The impact of a modest absorption coefficient $\alpha = \kappa_a/\kappa_T = 0.01$ is clearly visible in the form of a rapidly decaying profile extending out to about $t = 300$ only. In absolute numbers, the maximum of the lower curve is reduced to $\exp(-50\alpha) = 0.6$ times the magnitude of the absorption free profile. We have scaled the maxima of the two profiles to the same magnitude. The agreement with Monte Carlo is excellent.
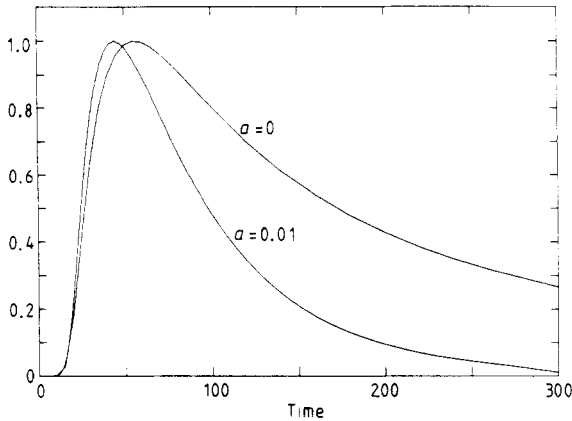
Figure 12. Illustration of the impact of a modest absorption coefficient $a = 0.01$. The geometry is semi-infinite with $\tau_0 = 10$, $\alpha = 0.05$ and $\tau = 0$. The upper curve shows the analytical sum P_0-P_{299} for $a = 0$. The lower curve shows the same sum for $a = 0.01$.

Acknowledgments

References

Code A D 1970 *Astrophys. J.* **159** 1029
Guilbert P W 1981 *Mon. Not. R. Astron. Soc.* **197** 451
Kennard E H 1938 *Kinetic Theory of Gases* (New York: McGraw-Hill)
Kunasz P B 1983 *Astrophys. J.* **271** 321
Nagel W and Mészáros P 1985 *J. Quant. Spectrosc. Radiat. Transfer* **34** 493
Pozdnyakov L A, Sobol I M and Sunyaev R 1977 *Sov. Astron.* **21** 708
—— 1979 *Sov. Astron. Lett.* **5** 149
Schultz A L and Price R H 1985 *Astrophys. J.* **291** 1
Schweizer M A 1987 *J. Phys. A: Math. Gen.* **20** 163